Combined Cloud–Microwave Radiative Transfer Modeling of Stratiform Rainfall

PETER BAUER

German Remote Sensing Data Center, German Aerospace Center, Cologne, Germany

A. KHAIN AND A. POKROVSKY

Institute of Earth Sciences, The Hebrew University of Jerusalem, Jerusalem, Israel

R. MENEGHINI AND C. KUMMEROW

NASA Goddard Space Flight Center, Greenbelt, Maryland

F. MARZANO

Dipartimento di Ingegneria Elettrica, Universita dell Aquila, L'Aquila, Italy

J. P. V. POIARES BAPTISTA

Electromagnetics Division, European Space Agency/ESTEC, Noordwijk, Netherlands

(Manuscript received 16 June 1998, in final form 14 May 1999)

ABSTRACT

The simulation of explicit particle spectra during cloud evolution by a two-dimensional spectral cloud model was used to investigate the response of microwave radiative transfer to particle spectra development with special focus on the radiative effects of melting particles below the freezing level. For this purpose, 1) a particle-melting model was implemented with increased vertical resolution; 2) several models of the dielectric permittivity for melting particles were compared; 3) the dependence on size–density distributions was evaluated; and 4) the influence on the results by the replacement of explicit by parameterized particle spectra was tested.

Radiative transfer simulations over ocean background at frequencies between 10.7 and 85.5 GHz showed a considerable increase in brightness temperatures (T_B) once melting particles were included. The amounts were strongly dependent on the implemented permittivity model, the number concentrations of large frozen particles right above the freezing level, and the local cloud conditions. Assuming a random mixture of air, ice, and meltwater in the particle, T_Bs increased by up to 30 K (at 37.0 GHz) in the stratiform cloud portion for nadir view. If the meltwater was taken to reside at the particle boundaries, unrealistic T_B changes were produced at all frequencies. This led to the conclusion that for large tenuous snowflakes the random-mixture model seems most appropriate, while for small and dense particles a nonuniform water distribution may be realistic. The net melting effect on simulated T_Bs, however, depended strongly on attenuation by supercooled liquid water above the freezing level, which generally suppressed the signal at 85.5 GHz. Over land background, changes in T_B due to melting particles remained below 8 K, which would be difficult to identify compared to variations in surface emission and cloud profile heterogeneity.

Replacement of the explicit particle spectra for rain, snow, and graupel by parameterized spectra (here, in exponential form with a fixed intercept) produced reductions of the melting signature by up to 40% over ocean. It was found that exponential size distribution formulas tended to underestimate number concentrations of large particles and overestimated those of small particles at those cloud levels where sufficient particle sedimentation leads to collection, aggregation, and evaporation, respectively. Consequently, the strongest differences between explicit and parameterized spectra occurred right above the freezing level for snow and graupel, and close to the surface for rain. Radiometrically, this resulted in an underestimation of scattering above the freezing level and an underestimation of emission by melting particles below the freezing level as well as by rain toward the surface. In the stratiform region, the net effect was a reduction of the melting signature; however, T_B's were still up to 15 K higher than from the no-melting case for the random-mixture permittivity model.

Corresponding author address: Dr. Peter Bauer, German Remote Sensing Data Center, German Aerospace Center, Linder Höhe, 51147 Köln, Germany.
E-mail: peter.bauer@dlr.de

1. Introduction

Apart from the long-term research of melting layer simulations in the framework of radar rain retrieval

methods, the effect of melting particles on passive microwave emission in the frequency range of currently employed airborne and spaceborne sensors (10–100 GHz) has not received much attention. Those few studies dealing with this subject from the modeling perspective find, however, that the melting effect contributes significantly to microwave emission from stratiform clouds and thus can cause errors in the hydrometeor retrieval methods if not included in the procedure (Vivekanandan et al. 1990; Schols et al. 1999; Bauer et al. 1999). Approaching the discussion from the other end leads to case studies where actual observations seem to be explained only by the presence of melting particles and where the exclusion of melting particles yields mismatches between the predicted and measured radiances (e.g., Schols et al. 1995; Schols et al. 1999). Nonetheless, there is a lack of both theoretical and experimental studies dealing with the significance of the radiative effects caused by melting hydrometeors.

One of the major problems, when more detailed models are used, is the introduction of many more degrees of freedom—that is, the assessment of a particle-melting model consistent with the assumptions of the cloud composition, a mixed-particle permittivity model, particle spectra development during melting, etc. (e.g., Schols et al. 1999; Bauer et al. 1999). For example, Meneghini et al. (1997) noted that small changes in the median diameter of the chosen particle size distribution function to those obtained from solving the radar equation may lead to significant uncertainties in the prediction of brightness temperatures.

This paper was prompted by the results of Bauer et al. (1999), which showed a significant contribution of melting particles to microwave radiances when measurements by airborne and spaceborne passive microwave sensors are simulated. However, many degrees of freedom are involved in the proper assessment of the melting environment so that a data source is required that reduces the uncertainty to that of particle composition. The presented study aims at the consistent description of the radiative effects of melting hydrometeors. For this purpose, we focused on a case study under extratropical conditions for which cloud model data were available with explicitly prescribed size spectra. A forthcoming investigation, based on multiple datasets from different cloud models and simulation experiments, will attempt to generalize the results presented here to tropical conditions. Furthermore, improved retrievals of hydrometeor and latent heating profiles, including aspects of three-dimensional cloud geometry and spatial sensor resolution, will conclude the current investigations.

A summary of the cloud model is presented in section 2a. The treatment of particle melting is described in section 2b. Section 3 outlines the modeling of particle composition and dielectric permittivity as a function of the composition of the particle and also describes the radiative transfer code employed. In section 4 radar reflectivity and multifrequency brightness temperature simulations are shown and investigated for various model and background configurations once the original cloud model size distributions are specified. For the assessment of the effect of parameterized size distributions, analogous radiative transfer calculations were carried out and are compared. Finally, a discussion of the results is presented.

2. Modeling of hydrometeor distributions

a. Cloud model

Simulations from a two-dimensional cloud ensemble model were used as input for the radiative transfer simulations (Khain and Sednev (1996). The model is based on a nonhydrostatic equation system of deep convection, the vertical size of the computational domain being 16 km. The horizontal size of the model grid and the horizontal resolution depend on the phenomena to be simulated. The variables of the model are: wind velocity, virtual potential temperature, water vapor mixing ratio, the number density distribution function for cloud condensation nuclei (CCN), and seven number density distribution functions (for water drops, three types of ice crystals—namely, columns, plates, dendrites—as well as snowflakes, graupel, and hail).

The description of microphysical processes is based on solving kinetic equations for the size distribution functions for water drops and ice particles. The model contains 33 mass categories both in the drop spectrum and in the spectra of ice particles. Figure 1a shows the mass-dependent density distributions for all particles as well as a mass–density distribution for snow, from Klaassen (1988), required for sensitivity studies in sections 3 and 4. Additionally, the particle diameters for categories water, snow, and graupel are presented in Fig. 1b, which are calculated from mass and density. The snow size–density distributions suggest that snowflake diameter differences between a factor of two and three can be expected to cause significantly different radiative signatures.

The model takes into account the following microphysical processes: activation of CCN and ice nuclei; condensational growth–evaporation of droplets; growth–sublimation of ice particles due to accretion; freezing of drops; melting of ice; coalescence among drops, among drops and ice particles, and among ice particles; ice multiplication; riming of snow; different regimes of droplets and ice sedimentation, which determine their terminal fall velocities; and breakup of drops and snowflakes.

The presented cloud model simulation describes the evolution of cloud patterns associated with coastal circulation in the eastern Mediterranean Sea during a rain event in the cold season when sea surface temperature is about 5 K higher than the land surface temperature. The computational area contains 65 grid points in the

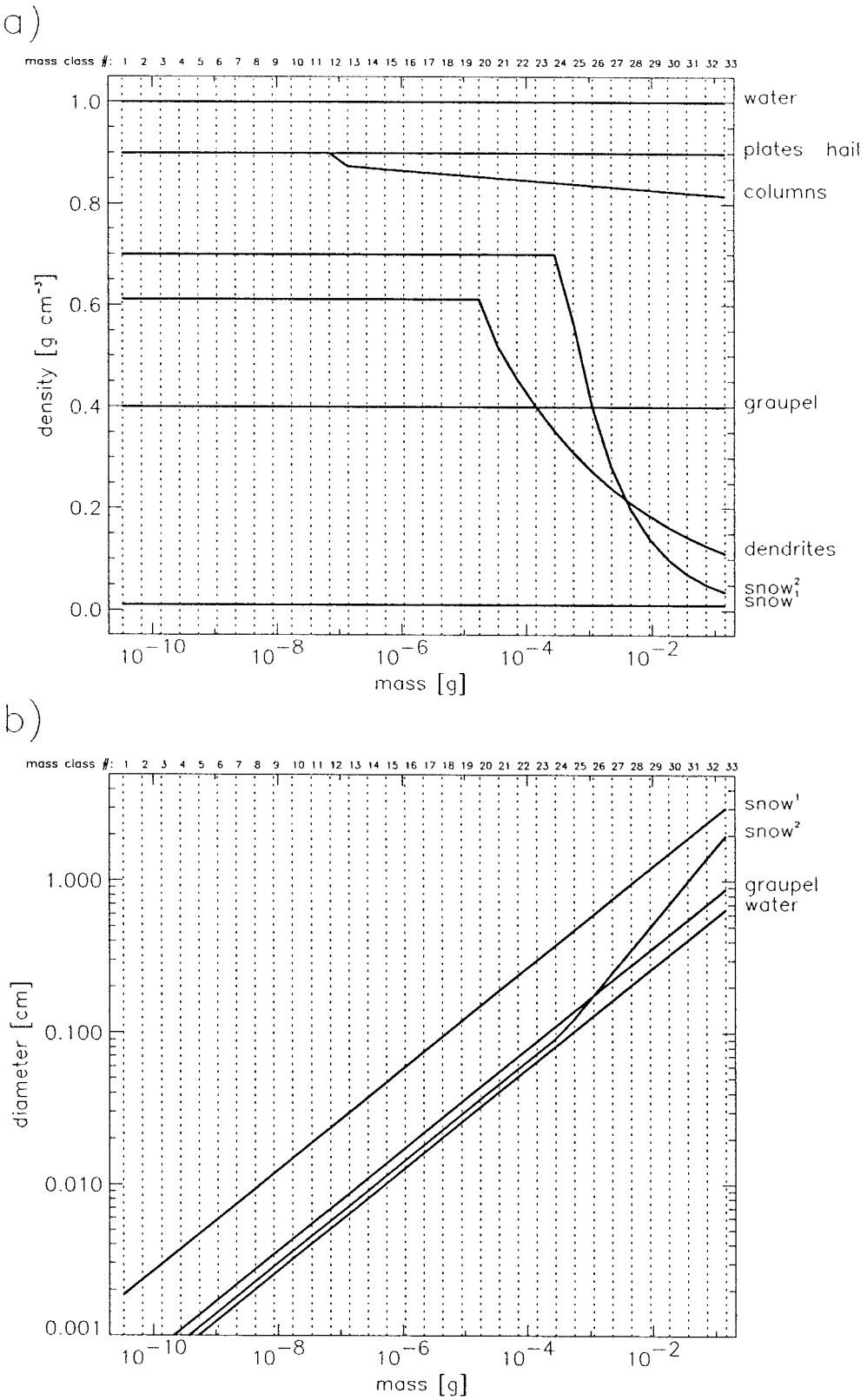

FIG. 1. (a) Cloud model inherent mass–density and (b) calculated mass–size distributions for seven hydrometeor classes [^{1} original distribution, ^{2} parameterized according to Klaassen (1988)]. Numbers indicate spectral mass classes.

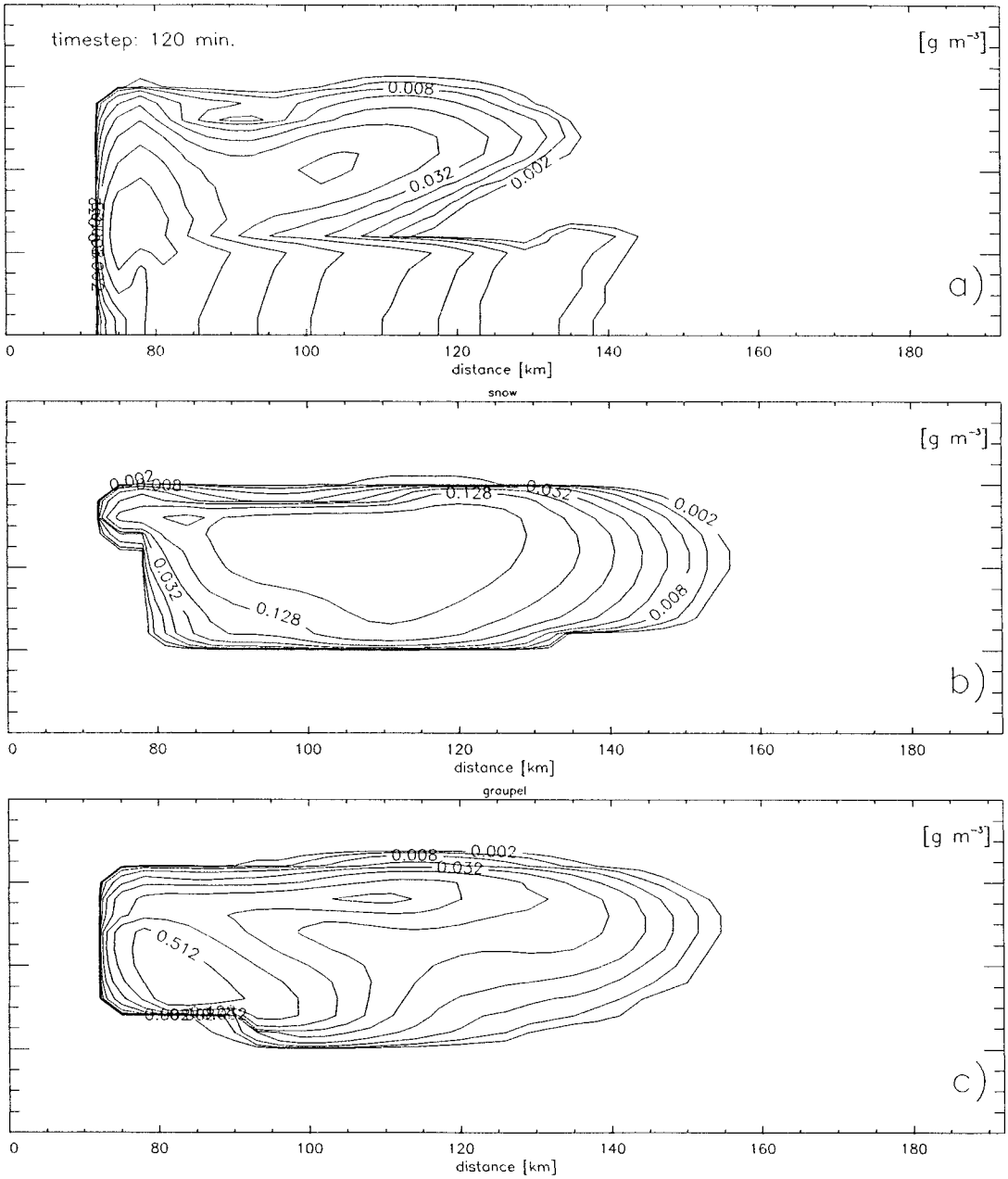

FIG. 2. Liquid/ice water contents for (a) rain, (b) snow, and (c) graupel at model time step $t = 120$ min.

horizontal and 41 layers in the vertical with grid spacings of 3 and 0.4 km, respectively. In the cloud model simulation, for $x < 75$ km the surface was assumed to be sea, while for $x > 75$ km a land surface was taken. The background wind is along the positive x direction so that a land–breeze type circulation is formed. Interaction of westerly wind and coastal circulation leads to the formation of a convergence zone a few kilometers offshore and to a persistent cloud formation at this location. The clouds are transported by the wind toward the land. Precipitation formation over land is determined by both drops (warm rain) and melting-ice particles. Thus the changes of the microphysical structure from shallow convective to stratiform take place in positive x direction.

During cloud evolution, clouds form at $t = 30$ min. For our analysis, cloud model simulations at time steps $t = 90$, 120, 160, and 180 min were selected, which show significant rain formation. They mainly differ by rain intensity in the stratiform portion of the cloud field. A detailed description of this case is given by Khain et al. (1996). For illustration, Figs. 2 and 3 show the liquid water and ice contents of precipitating drops ($r > 0.1$ mm), snow, and graupel over the model domain for the

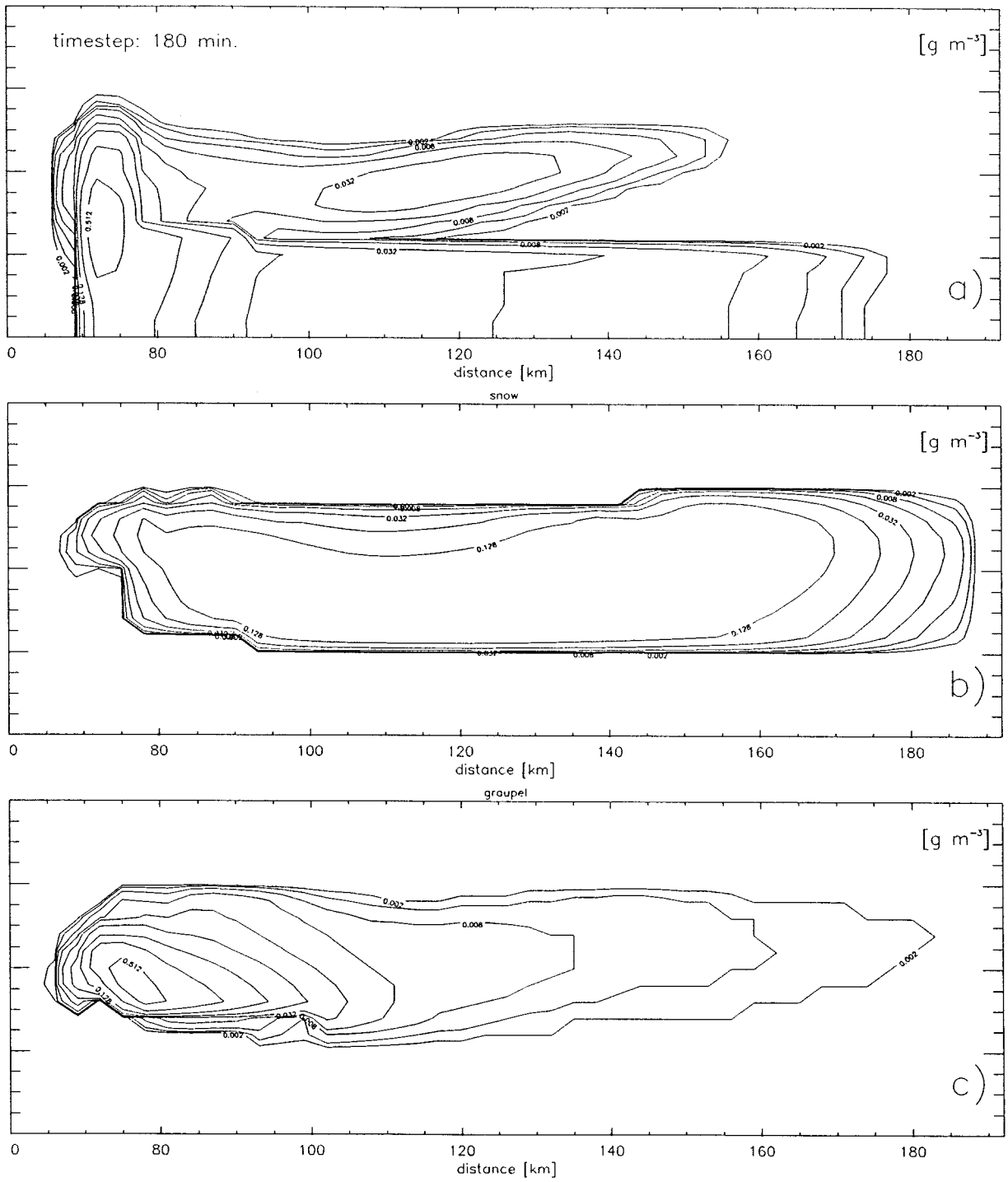

FIG. 3. Same as Fig. 2 but at $t = 180$ min.

time steps after initiation and the largest extent of the stratiform cloud component. Note that significant amounts of supercooled water are present, injected to altitudes above the freezing level by the convection above the coastline, which drifted over land by the westerly winds.

b. Particle-melting model

Usually, the transfer of frozen particles into raindrops that precipitate through the melting layer is simply modeled as a function of penetration depth, that is, depth below the 0° isotherm. From radar sensitivity studies

(e.g., Wexler 1995) two different groups of parameters emerge, which for radiative transfer purposes, usually suggest the inclusion of first-order parameters responsible for the radar reflectivity in the melting layer, that is, particle permittivity as a function of fractional melting water and fall speed as a function of particle size. Second-order parameters such as particle shape and particle interactions seem to have less significant impact.

Following the model used by Bauer et al. (1999), two different approaches to individual particle melting were tested, motivated by the strong dependence of melting speed on particle size and, in particular, particle density. Our previously employed size–density relation of Magono and Nakamura (1965) seems to suffer from a general overestimation of melting speed caused by densities at large particle radii that are too low, which caused particles bigger than a critical size to melt more rapidly than smaller particles.

Figures 4a and 4c show an intercomparison of different melting model performances assuming a constant snow particle density of 0.01 g cm^{-3} as prescribed by the cloud model, while Figs. 4b and 4d show corresponding results when particle density is reduced with increasing diameter, D_s (in cm), that is, $\rho_s = \min(0.7, 0.07/D_s)$ g cm^{-3} (see snow²-distribution in Fig. 1, also see Klaassen 1988). In this example, a temperature lapse rate of 6 K km^{-1} and a constant relative humidity of 90% were used. The graphs illustrate the dependence of meltwater mass on distance below the freezing level (FL) and particle diameter (i.e., a value of 1 indicates a completely melted particle). The prognostic model equations were translated into distance-below-FL-dependent equations, respectively. The first model is reproduced here from Rutledge and Hobbs (1983):

$$\frac{dm_m}{dz}V_m(D_m) = \frac{2\pi D_s}{L_f}K_a(T - T_0)(0.65 + 0.44S_c^{1/3}R_e^{1/2}). \quad (1)$$

The meltwater mass of the particle is denoted by m_m; z is the altitude below FL, which can be used to calculate the meltwater fraction using the mass of the frozen particle at FL. The expression $V_m(D_m)$ denotes the terminal fall speed of the melting particle with diameter D_m; L_f the latent heat of water fusion ($=3.3410^5$ J kg^{-1}); K_a the thermal conductivity of air ($=2.4310^{-2}$ J m^{-1} s^{-1} K^{-1}); D_s the diameter of the frozen particle; T the temperature; T_0 the temperature at FL; S_c the Schmidt number ($=0.6$); and $R_e = V_s(D_s)D_s\rho/\mu$ the Reynolds number, with terminal fall speed of the frozen particle of diameter D_s, V_s, air density ρ, and dynamic viscosity of air $\mu = 1.718\ 10^{-5}$ kg m^{-1} s^{-1}. Evaporative cooling has been neglected so that T always denotes both particle and ambient temperature; that is, particle temperature is the same as of the ambient air at the same level. The terminal fall speed of the melting particle is calculated from $V_m(D_m) = V_w(D_w)(D_w/D_m)$ (Dissanayake and McEwan 1978), with terminal fall speed of the melted particle, V_w, of diameter D_w.

The second melting model follows Mitra et al. (1990), which was unified with (1) with respect to units and notation. This model was employed for spherical particles; thus:

$$\frac{dm_m}{dz}V_m(D_m) = \frac{2\pi D_s}{L_f}(a + b\chi^c) \times \left[K_a(T - T_0) + \frac{D_v L_e M_w}{R}\left(\frac{\Phi_v e_s(T)}{T} - \frac{e_s(T_0)}{T_0}\right)\right], \quad (2)$$

with $\chi = S_c^{1/3}R_e^{1/2}$, where coefficients, a, b, and c are defined dependent on χ, that is, for $\chi \leq 1$ then $a = 1$, $b = 0.14$, $c = 2$, while for $\chi > 1$ then $a = 0.86$, $b = 0.28$, $c = 1$. The second term in brackets includes particle evaporation with the diffusivity of water vapor in air, $D_v = 2.2610^{-5}$ m^2 s^{-1}; latent heat of evaporation, $L_e = 3.3410^6$ J kg^{-1}; molecular weight of water, $M_w = 18$ g mol^{-1}; ideal gas constant, $R = 8.314$ J mol^{-1} K^{-1}; relative humidity, Φ_v; and saturation water vapor pressure, e_s.

It is obvious from the conversion of time dependence into fall distance dependence that horizontal and vertical velocities have to be negligible so that mass conversion at certain altitude levels due to melting can indeed be explained by the melting process itself, excluding particle advection and convection. The vertical particle flux adjustment described in the following section also requires particle sedimentation prescribed by terminal velocities so that the above melting models are only applicable where environmental air motion is of minor importance.

The only differences between (1) and (2) are in the formulation of the ventilation coefficient and in the inclusion of particle evaporation in (2), which is treated separately in the equation system employed by Rutledge and Hobbs (1983). Comparison of Figs. 4a with 4c and Fig. 4b with 4d shows that both models produce almost identical results. Evaporation causes a continuous loss of melted water during particle sedimentation in the case of subsaturated air so that the accumulation of meltwater fraction is slowed down. A similar effect is caused by evaporative cooling, which was neglected in this case.

Particle density has a strong impact on the melting process. If particle density is parameterized as a function of diameter, dramatic changes in the melting behavior can be observed. With size-dependent density, as described above, the fall distance over which complete melting occurs doubles, thus producing a deeper melting layer (compare Figs. 4a and 4b or Figs. 4c and 4d). With respect to the radiative transfer calculations, the main effect can be expected to arise from particle size determination since, in our case, these are calculated from particle mass categories as prescribed by the cloud model. However, the melting process itself seems most com-

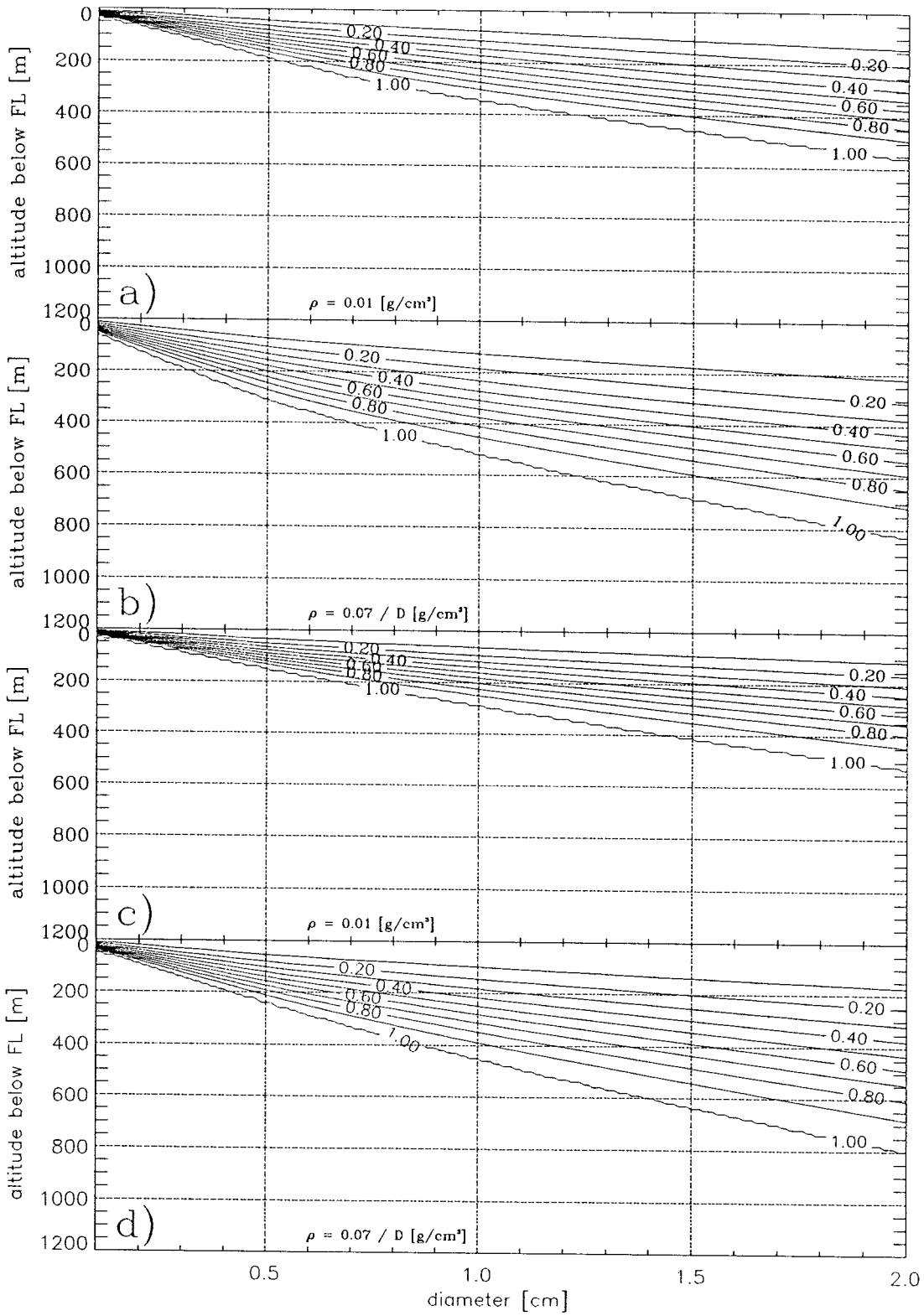

FIG. 4. Fractional amount of meltwater dependent on particle diameter, D_s, and fall distance below FL according to the models of Mitra et al. (1990) for particle density (a) $\rho_s = 0.01$ g cm^{-3}, (b) $\rho_s = 0.07/D_s$ g cm^{-3}, and (c), (d), Rutledge and Hobbs (1983) for the same densities.

pletely described by (2) so that it was employed for all further calculations.

c. Mass flux adjustment

Originally, the cloud model presented in section 2a did not explicitly calculate a melting-particle mass because of its rather coarse vertical resolution; that is, a direct and total conversion of snow into rainwater was assumed within the first layer below the 0°C isotherm. To allow a proper implementation of the melting model, the vertical resolution had to be synthetically increased by interpolation of all parameters to 40-m grid spacing. The consistency of this with the cloud model was ensured by an adjustment of particle spectra at intermediate cloud layers below the FL with the requirement that mass fluxes would not be discontinuous at the predefined levels. Thus an interpolation of mass flux (in m s^{-1}), PMF, here defined as

$$\mathrm{PMF}(z) = \frac{1}{\rho_w} \sum_{i=1}^{N_c} \sum_{j=1}^{N_m} V_{ij}(m_j, z) N_{ij}(m_j, z) m_j \, \Delta m_j, \quad (3)$$

between the FL and the levels below, was introduced. The V_{ij} denotes the terminal fall velocity of a particle of mass m_j and number density N_{ij} (in m^{-3} g^{-1}), where N_m is the number of mass bins and N_c the number of particle categories. The term ρ_w denotes the water density. For homogeneous particles the V_{ij} were computed using the formula also employed in the cloud model (Khain and Sednev 1995).

PMF interpolation had to be carried out for layers below the FL without violating the cloud model framework at those levels where not all particles are completely melted. Consequently, a redistribution of meltwater into frozen particle categories was required so that this ice could be melted, requiring a conservation of the overall mass flux. Since liquid precipitation is often present above the FL, the particle spectra had to be interpolated to match the fluxes of the frozen precipitation above the FL and the liquid precipitation below the FL that is not contributed by the liquid precipitation above FL. The latter can be defined as

$$\mathrm{PMF}'_w(z_{k-1}) = \mathrm{PMF}_w(z_{k-1}) - \mathrm{PMF}_w(z_k), \quad (4)$$

where level z_k denotes the FL and z_{k-1} denotes the next lower model level below the FL where all frozen particles were melted in the original model simulation. Then, the mass flux available for melting, PMF_m, was calculated at intermediate levels, z_l, from interpolation between the frozen mass flux at FL, $\mathrm{PMF}_i(z_k)$, and $\mathrm{PMF}'_w(z_{k-1})$ by

$$\mathrm{PMF}_m(z_l) = \mathrm{PMF}_i(z_k) + \frac{\mathrm{PMF}'_w(z_{k-1}) - \mathrm{PMF}_i(z_k)}{z_{k-1} - z_k}(z_l - z_k). \quad (5)$$

In the stratiform portion the differences between PMF'_w below and PMF_i right at FL are rather small; thus the slope of the interpolation in (5) is flat. This corresponds well with the a priori assumption of general flux conservation throughout the profile below the FL. This is valid, however, only if vertical velocities are rather constant. Exclusion of profiles with strong updrafts and large variations in the vertical particle flux profiles limited the application of (5) to profiles at $x > 85$ km. Outside, no adjustment was applied and the profiles remained in the original state.

d. Parameterized size spectra

Since spectral cloud model simulations are computationally expensive, it is worthwhile to investigate the effect of the replacement of the original particle spectra by parameterized spectra. This replacement allows us to assess the accuracy of the procedure for radiative transfer studies and to test whether the results can be generalized to include the effects of melting. If differences are small, the presented methodology can be transferred to simulations from three-dimensional cloud ensemble models with parameterized particle spectra to improve databases for hydrometeor retrievals from aircraft and satellite data.

For this purpose, spectra of rain, snow, and graupel were approximated by exponential size distribution functions of the form:

$$N(D) = N_0 \exp(-\Lambda D)\, dD, \qquad \Lambda = \left(\frac{\pi \rho_w N_0}{\mathrm{LWC}}\right)^{1/4}, \quad (6)$$

with particle number concentration $N(D)$ (in cm^{-4}) at diameter D in the interval dD. All parameters depend on the category of particle species, that is, rain, snow, or graupel (hail was neglected here due to low concentrations mainly in the vicinity of the convective cell). The D denotes the particle diameter (in cm), N_0 the intercept of the distribution function (in cm^{-4}), and LWC either the liquid or ice water content (in g m^{-3}) (e.g., Rutledge and Hobbs 1983). Here, N_0 was assumed to be fixed at 0.08 cm^{-4} for rain, 0.04 cm^{-4} for both snow and graupel. This implies that the form of the spectra introduced by varying liquid/ice water contents only affects the slope of the distribution. For better estimation of the errors, the parameterized spectra were limited to those mass intervals, truncated elsewhere, where the explicit model gave particle number concentrations other than zero. The cloud hydrometeor spectra were calculated in terms of mass categories so that the transformations $N(m)\, dm = N(D)\, dD$ and $D^3 = 6m/(\pi\rho)$ were applied as obtained from the organization of the mass increments and integration over spectra according to Berry and Reinhardt (1974).

3. Modeling of radiative transfer

a. Particle permittivity

The effective permittivity is calculated as a function of the individual contributions by water, ice, and air.

Their impact on effective particle permittivity and modeled radar reflectivity excess were discussed by Klaassen (1988). The analysis shows that extreme discrepancies occur among different approaches, in particular for low particle contents in the volume right after the onset of melting. Comparing the classic Maxwell–Garnett (MG; in Bohren and Battan 1982) formulations for fixed-mixture constellations, such as a water matrix with ice inclusions (MG_{wi}) or vice versa (MG_{iw}), with experimental studies (e.g., Mitra et al. 1990) leads to the conclusion that these formulas may describe realistic dielectric particle properties only at certain melting stages but do not apply to all configurations during particle melting. This was also confirmed by a study of Meneghini and Liao (1996) who reviewed available models. Their main conclusion is that the Maxwell–Garnett formulation for an air–ice mixture in a water matrix compared best to their fast Fourier transform numerical method applied to a mixed particle when the ice volume fraction was below 0.2. For larger fractions of melting water all models showed similar results. These conclusions were based on the assumption that both water and ice cells were distributed randomly over the particle volume. Once the meltwater was accumulated at the particle surface, its permittivity reached values similar to a water-coated particle, which is well represented by MG_{wi}. Meltwater location, in turn, depends on initial particle density and melting stage, so that different models may apply to various melting stages.

For the spatially random ice–water mixture (denoted ML96; see Meneghini and Liao 1996), the authors developed an analytical function to better represent the complex particle permittivity, ϵ_{mix}, at 7.7 GHz and intermediate melting stages using an error function to interpolate between MG_{wi} and MG_{iw} as a function of fractional volume of ice, f_{vi}, respectively. Even though the application of this model to other frequencies may not seem justified, the effective permittivity calculation is driven by the weights obtained from the error function that are closely tied to MG_{iw} at early melting stages and thus represent a rather conservative estimate of the particle permittivity.

Recently, Meneghini and Liao (1998) and Meneghini and Liao (2000, hereafter ML00) improved the generality of the calculations by employing a continuous multiple-components particle approach with parameterizations that allow its application to frequencies between 10 and 95 GHz. This model is based on the assumption that the properties of the constituents are homogeneous, isotropic, and linearly superimposed, so that

$$\epsilon_{\text{mix}} = \frac{\epsilon_w f_w \dfrac{\langle E_w \rangle}{\langle E_i \rangle} + \epsilon_a f_a \dfrac{\langle E_a \rangle}{\langle E_i \rangle} + \epsilon_i f_i}{f_w \dfrac{\langle E_w \rangle}{\langle E_i \rangle} + f_a \dfrac{\langle E_a \rangle}{\langle E_i \rangle} + f_i}, \tag{7}$$

where ϵ_w, ϵ_a, and ϵ_i represent the permittivities of water, air, and ice with volume fractions f_w, f_a, f_i, requiring $f_w + f_a + f_i = 1$. The terms in brackets denote the average electric fields, assuming that a particle can be decomposed into individual cells over which the fields are homogeneous so that the summation of all cell contributions to the total field is equivalent to the average field multiplied by the number of cells. The ratio of average electric field $\langle E_a \rangle / \langle E_i \rangle$ in (7) is computed from the Debye formula, assuming a dry snow particle with $f_i' + f_a' = 1$, and densities of snow, air, and ice, ρ_s, ρ_a, ρ_i:

$$\frac{\langle E_a \rangle}{\langle E_i \rangle} = \frac{f_i'(\epsilon_s - \epsilon_i)}{f_a'(\epsilon_a - \epsilon_s)}, \qquad \epsilon_s = \frac{\rho_i + 2k_i\rho_s}{\rho_i - k_i\rho_s},$$

$$k_i = \frac{\epsilon_s - 1}{\epsilon_s + 2}. \tag{8}$$

Finally, both real and imaginary parts of $\langle E_w \rangle / \langle E_i \rangle$ were computed by the conjugate gradient numerical method and parameterized in wavelength and fractional meltwater.

Figure 5 shows the real versus imaginary part of the dielectric permittivity at four frequencies for ice volume fraction between unity (low values) and zero (high values) assuming initial snow densities of 0.01 g cm^{-3} (Figs. 5a–d) and 0.5 g cm^{-3} (Figs. 5e–h), respectively. The MG configurations show the dominance of the respective contribution from the material chosen as the matrix, which seems unrealistic when applied to cloud particles at least at those melting stages where 1) melting begins and a water matrix was assumed or 2) melting is almost complete and an ice matrix was assumed. ML96 is mainly driven by those parameters determining the error function impact, which is obvious from the relatively drastic switch between states close to MG_{wi} or MG_{iw}. The large symbols indicate the permittivities at a meltwater mass fraction of 50%. From this indication it becomes obvious that ML96 is identical to MG_{iw} well beyond a 50% ice mass fraction at all frequencies and initial particle densities. Thus, as for MG_{iw}, a weak radiative effect of melting particles can be expected for this model unless particle concentrations would become very high. Even though the permittivities reach values close to those of MG_{wi} at later stages, the particles are almost completely melted (thus too small) to produce significant emission. ML00 can be regarded as close to the average of MG_{wi} and MG_{iw}. Table 1 gives an overview.

b. Radiative transfer model

Plane-parallel simulations of radiances emitted by stratiform clouds at frequencies of the Special Sensor Microwave/Imager (SSM/I) and the Tropical Rainfall Measuring Mission (TRMM) Microwave Imager (TMI) and both polarizations were carried out (here, only shown: 10.7, 19.35, 37.0, and 85.5 GHz) by use of the Eddington approximation to radiative transfer (e.g., Kummerow 1993). In order to estimate the relative ef-

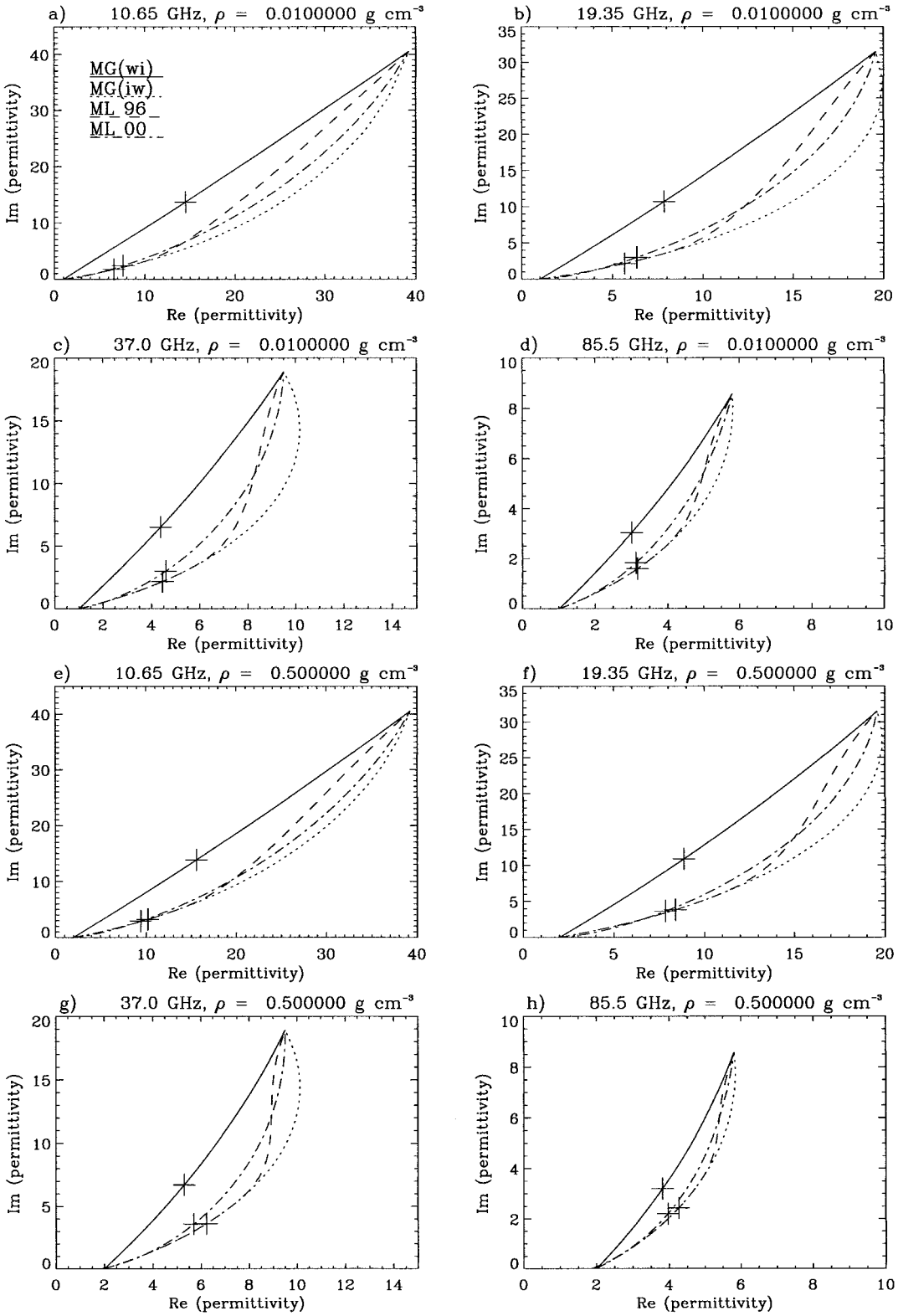

FIG. 5. Complex dielectric permittivity for melted water volume fractions between 0 and 1 for a spherical snow particle with density 0.01 g cm^{-3} at (a) 10.7 GHz, (b) 19.4 GHz, (c) 37.0 GHz, and (d) 85.5 GHz; (e)–(h) like (a)–(d) for particle density of 0.5 g cm^{-3}. Permittivity models are described in the text; symbols mark meltwater fraction of 50%.

TABLE 1. Permittivity model summary.

Model	Composition	Effects with respect to melting particles
MG_{wi}	Ellipsoidal inclusions (ice) randomly distributed in a homogeneous matrix (water).	Water contribution dominates for all meltwater fractions. Initial particle type/size becomes important.
MG_{iw}	Ellipsoidal inclusions (water) randomly distributed in a homogeneous matrix (ice).	Ice contribution dominates until late melting stages. Almost no effects.
ML96	Random ice–water mixtures (quasi-spherical).	Ice contribution dominates for meltwater fractions <0.7. Significant effects only for very large particles.
ML00	Random air–ice–water mixtures (low eccentricities).	Close to average between MG_{wi} and MG_{iw}.

fect of melting particles on the emission, the simulations were performed by either including or excluding the melting process. When melting was not included, the frozen particles were assumed to be melted completely at all altitudes below FL. In the following, brightness temperature differences (ΔT_Bs) refer to T_Bs from simulations with a melting and permittivity model of some kind minus simulations without melting.

Atmospheric absorption was calculated following Liebe et al. (1992). The properties of cloud and rain ice and water particles were computed from Lorenz–Mie theory. The sea surface emissivity parameterization of Schluessel and Luthardt (1991) as a function of temperature and near-surface wind speed was applied for the lower boundary. When a land surface was assumed a simplified, spectrally dependent emissivity (allowing for inclusion of vegetation, roughness, soil moisture, and temperature effects) was implemented (Bauer and Grody 1995).

4. Results

To identify contributions from both surface and melting hydrometeors as well as cloud geometry effects, several configurations were installed.

1) Cloud model simulation including, versus excluding, melting over a homogeneous ocean surface for nadir view and inclined view at zenith angle $\theta = 53°$. The inclined sensor-viewing geometry was simulated applying the Modified Eddington Model as described in Bauer et al. (1998).
2) Cloud model simulation including, versus excluding, melting over original land–sea distribution (land surface for $x > 75$ km) for nadir view.

Figures 6–8 show examples of extinction coefficients at 37.0 GHz and equivalent radar reflectivity at 13.8 GHz for model cloud time step $t = 160$ min. when either ML96 (Fig. 6), ML00 (Fig. 7), or MG_{wi} (Fig. 8) was implemented. As predicted by the particle permittivity calculations in section 3a, ML96 produces comparably low extinction coefficients up to 0.2 km^{-1} in the melting layer, which are more than three times lower than those computed by ML00. Radar reflectivities seem to be low as well, indicated by values up to 35 dBZ when ML96 is used. The melting layer is reasonably expressed in the reflectivity patterns produced by ML00 with maximum values of about 45 dBZ. In contrast, choosing MG_{wi}, extreme extinction coefficients ($\sim$3 km^{-1}) and radar reflectivities ($\sim$52 dBZ) are produced, which seem well above the expectations. However, since the model-inherent particle density is very low, this exaggeration by MG_{wi} is significantly reduced by increasing particle density. This changes both particle-melting behavior and cross sections. The melting process is slowed down, and frozen particles survive longer below the FL.

If the radiative transfer is modeled employing a decrease of snow density with size (not shown here) as described above, ML96 produces maximum extinction coefficients of 0.2 km^{-1} and reflectivities of 30 dBZ with no indication of a bright band, while ML00 generates maximum extinction coefficients of 0.65 km^{-1} and associated reflectivities of 35 dBZ in the melting region. Thus extinction coefficients change by a factor of two for ML00 once particles become more dense and particle sizes reduce significantly. Interestingly, the combination of the MG_{wi} particle permittivity model with the above density adjustment produces results almost identical to the combination of ML00 and low densities (thus very large particles) as presented in Fig. 7 for both extinctions at 37.0 and 85.5 GHz and radar reflectivities at 13.8 GHz. This leads to the conclusion that without knowledge of both particle size–density and particle composition, a proper assessment of melting layer effects is not possible if lower frequency radiometry is excluded. In this case, by optimizing the particle density–size distribution and permittivity model, measurements of reflectivity and emitted radiation could be reproduced without matching the actual microphysical conditions. On the other hand, these results suggest that if both low- and high-frequency emission is high, particles do not have to be very big but very wet to explain the observations. Conversely, if only high-frequency emission is increased, then particles may be large but not very wet. If the snowflake-melting sequence of Mitra et al. (1990) applies, particles in the second melting stage—that is, where the meltwater is

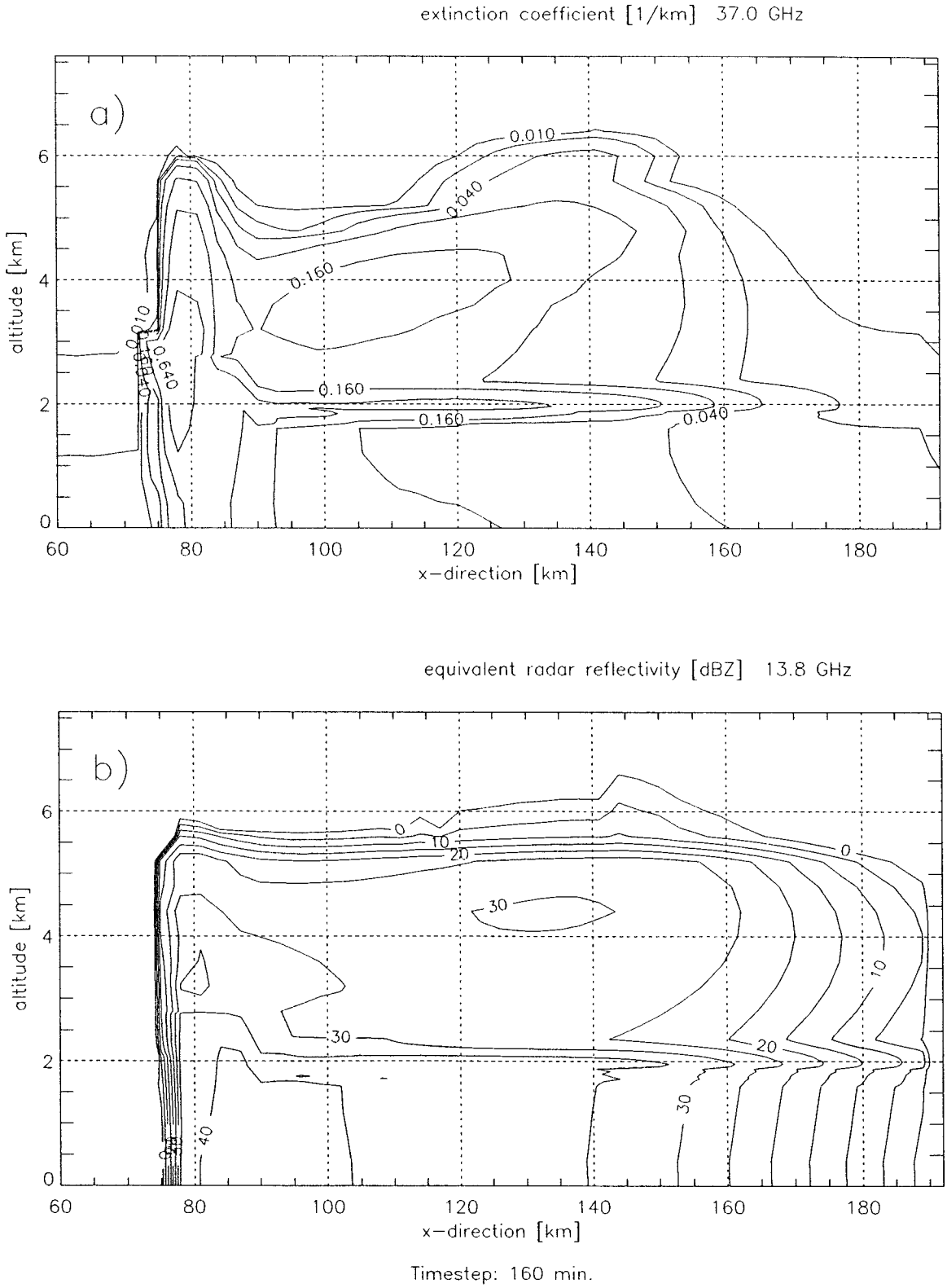

FIG. 6. Extinction coefficients at (a) 37.0 GHz and (b) equivalent radar reflectivities at 10.7 GHz and model time step t = 160 min, employing particle permittivity model ML96.

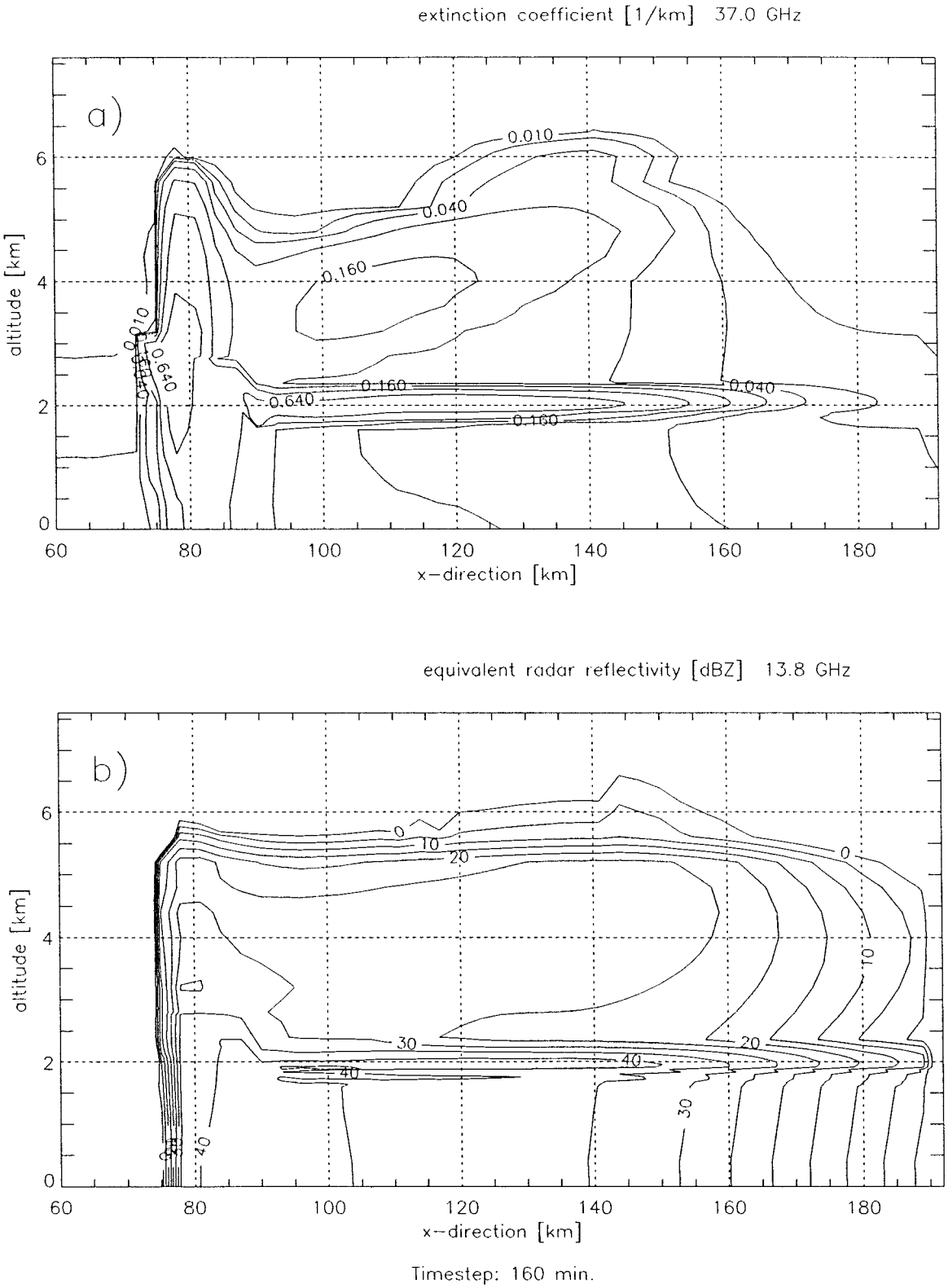

FIG. 7. Same as Fig. 6 but for ML00.

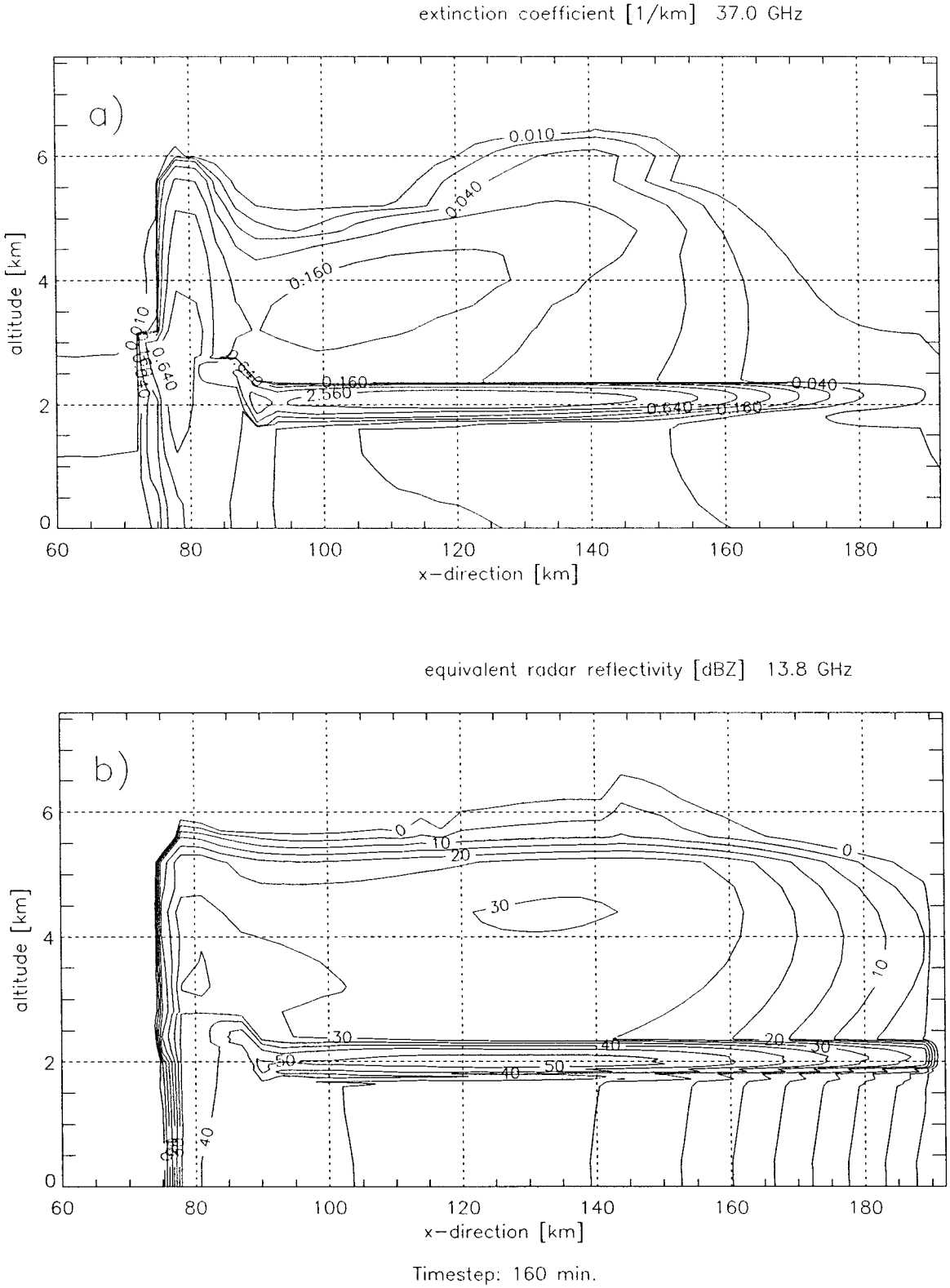

FIG. 8. Same as Fig. 6 but for MG_{wi}.

homogeneously distributed over the flakes' branch linkages and channels—would be present in this case.

a. Melting effect over ocean background

In Figs. 9a and 9b average brightness temperature differences ΔT_B over a homogeneous ocean background between simulations employing the explicit particle spectra (EDSD) and all permittivity models versus no melting are shown for nadir view. Figures 9c and 9d show the corresponding results for parameterized spectra (PDSD), which are discussed below, while Figs. 9e and 9f give average differences between EDSD and PDSD for the simulations with melting particles. The averages include all cloud model time steps at locations $x > 97$ km. Note, the associated standard deviations (not shown here) have similar amounts and spectral behavior as the averages. Figure 10 gives an example of the spatiotemporal distribution of ΔT_B for ML00 and EDSD. In summary, the following features appear.

- The ΔT_Bs are higher for low particle densities and thus bigger particles. The bigger the snow particles after the onset of melting, the stronger the excess emission compared to pure water particles of the same mass.
- The MG_{wi} always produces a much stronger signature than any other permittivity model because it resembles most the permittivity of pure water. This was already illustrated by Fig. 5 and Fig. 8. The amounts of average and maximum ΔT_B (120 K) suggest that MG_{wi} does not give realistic permittivities for large and tenuous snowflakes but, rather, holds for smaller and more dense particles such as graupel. This is in agreement with the results of Bauer et al. (1999).
- For MG_{wi}, the average ΔT_B decrease with increasing frequency. Since MG_{wi} produces the strongest increase in extinction, a saturation effect occurs at higher frequencies. This limits the further increase of T_Bs to lower frequencies, producing larger ΔT_B since ocean background T_Bs are lower. The suppression of ΔT_B due to the saturation effect is amplified by attenuation in overlying cloud layers, which increases with increasing frequency.
- For both mass-density distributions, ML96 and ML00 show, on average, no significant effect in ΔT_B below 37.0 GHz, and a small standard deviation (2 K). At 37.0 GHz, only ML00 produces a noticeable average ΔT_B of 10 K, with maximum values of 25 K (standard deviation 10 K). Thus, validity of ML96 would not give a clearly identifiable melting effect at all investigated frequencies and particle models.
- At $t = 180$ min, for example, ML00 generates the strongest signature at 37.0 GHz where particle fluxes are high (95 km $< x <$ 160 km) and at 85.5 GHz where upper cloud attenuation is weak ($x > 120$ km) (Fig. 10).
- Negative ΔT_B occur where strong vertical gradients of liquid particle fluxes right below the FL are present (between 80 and 100 km in Fig. 10). There, particle spectra above the FL show small numbers of large particles, which is inverted at the next lower level (see also Fig. 12g vs 12j). When the melting model is inserted, the transient conversion of the snow and graupel into melted spectra does produce less emission than the pure rain spectrum once ML96 or ML00 is used. The discontinuity in the liquid water profile is not exceeded by the melting effect unless MG_{wi} is used.

b. Melting effect over land background

Over a land background, the melting effect is obscured due to the high emissivity of the surface. Thus at lower frequencies where the cloud is less opaque, all computations showed ΔT_B below 1 K at 10.7 GHz, 5 K at 19.35 GHz, and 8 K at 37.0 and 85.5 GHz, respectively. These are generally below variations induced by surface parameters such as moisture, temperature, or roughness so that they cannot be identified independently. The importance of the particle permittivity model is reduced accordingly, which would become even more obvious if the model's spatial resolution were adjusted to satellite scales. Keeping in mind that usage of MG_{wi} has led to dramatic changes in brightness temperatures of up to 120 K over oceans, the negligible effect of MG_{wi} over land indicates that there is no significant sensitivity to melting and liquid precipitation at the investigated frequencies. Thus over land, only considerable scattering by ice particles aloft allows a rather indirect precipitation estimation.

c. Size distribution effects

Three profiles of particle spectra of liquid water, snow, and graupel at five different altitudes in the convective core at $x = 75$ km and model time step $t = 120$ min (Fig. 11) as well as in the stratiform region at $x = 93$ km and $t = 120$ min (Fig. 12) and at $x = 120$ km and $t = 180$ min (Fig. 13) have been selected for illustration.

Inside the convection and at all chosen altitudes, both rain- and graupel-explicit spectra seem well represented by the exponential functions, even though the ongoing warm rain generation at this time step leads to an under representation of large raindrops and over representation of small droplets in the liquid spectrum by the PDSD below the (FL Figs. 11g,j). In spite of this, an almost perfect match with the exponential distribution at the surface is evident (Fig. 11m). Different microwave signatures would only be produced by the insufficiently reproduced snow spectrum near the FL. An increase in particle aggregation results in a more narrow particle spectrum and an increase in the differences between the EDSD and PDSD. Here, lower T_Bs can be expected from

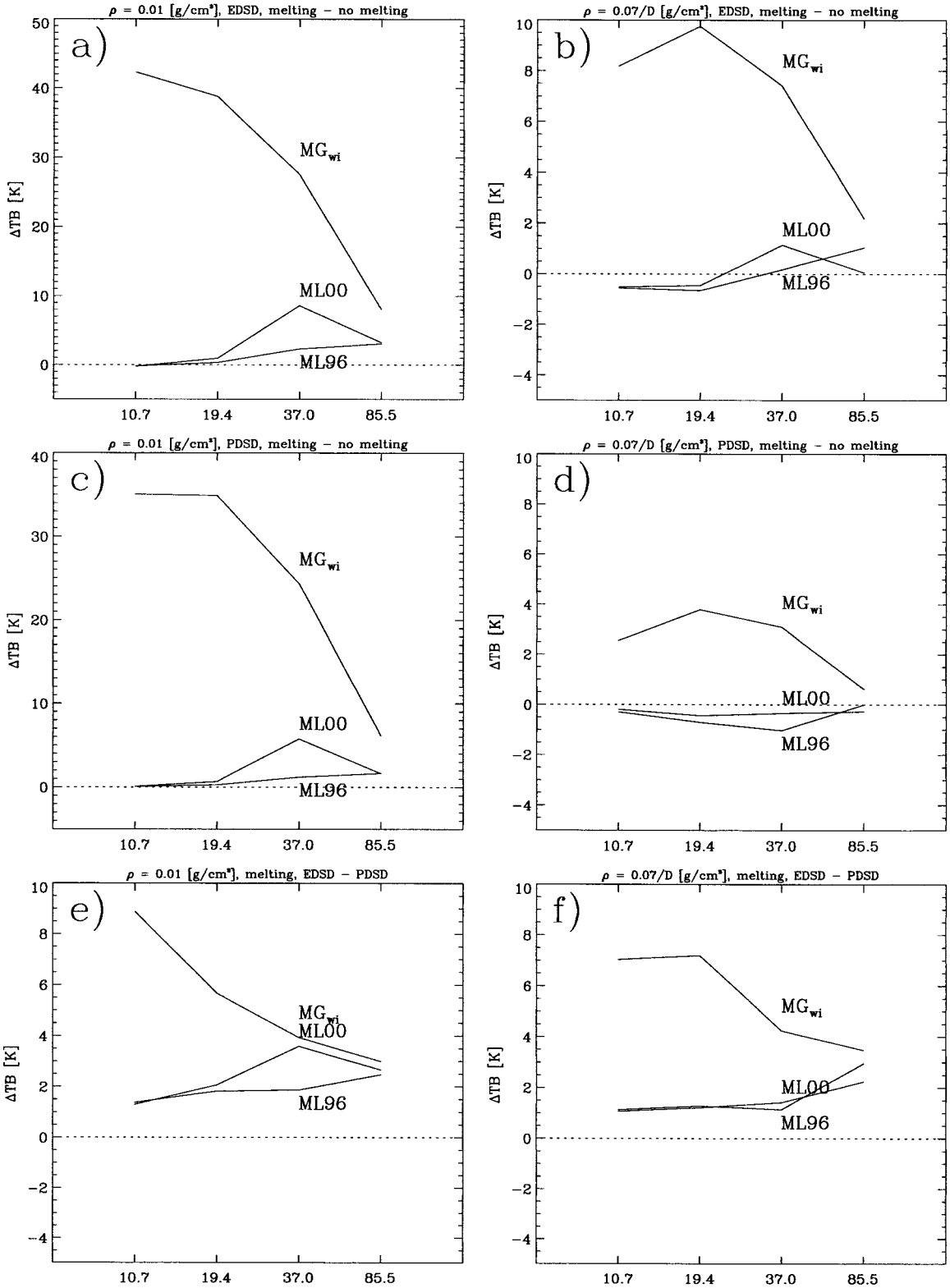

FIG. 9. Average ΔT_Bs for all permittivity models: EDSD, melting − no melting, and (a) $\rho_s = 0.01$ g cm^{-3} vs (b) $\rho_s = 0.07/D_s$ g cm^{-3}; PDSD, melting − no melting, and (c) $\rho_s = 0.01$ g cm^{-3} vs (d) $\rho_s = 0.07/D_s$ g cm^{-3}; EDSD − PDSD, melting − no melting, and (e) $\rho_s = 0.01$ g cm^{-3} vs (f) $\rho_s = 0.07/D_s$ g cm^{-3}.

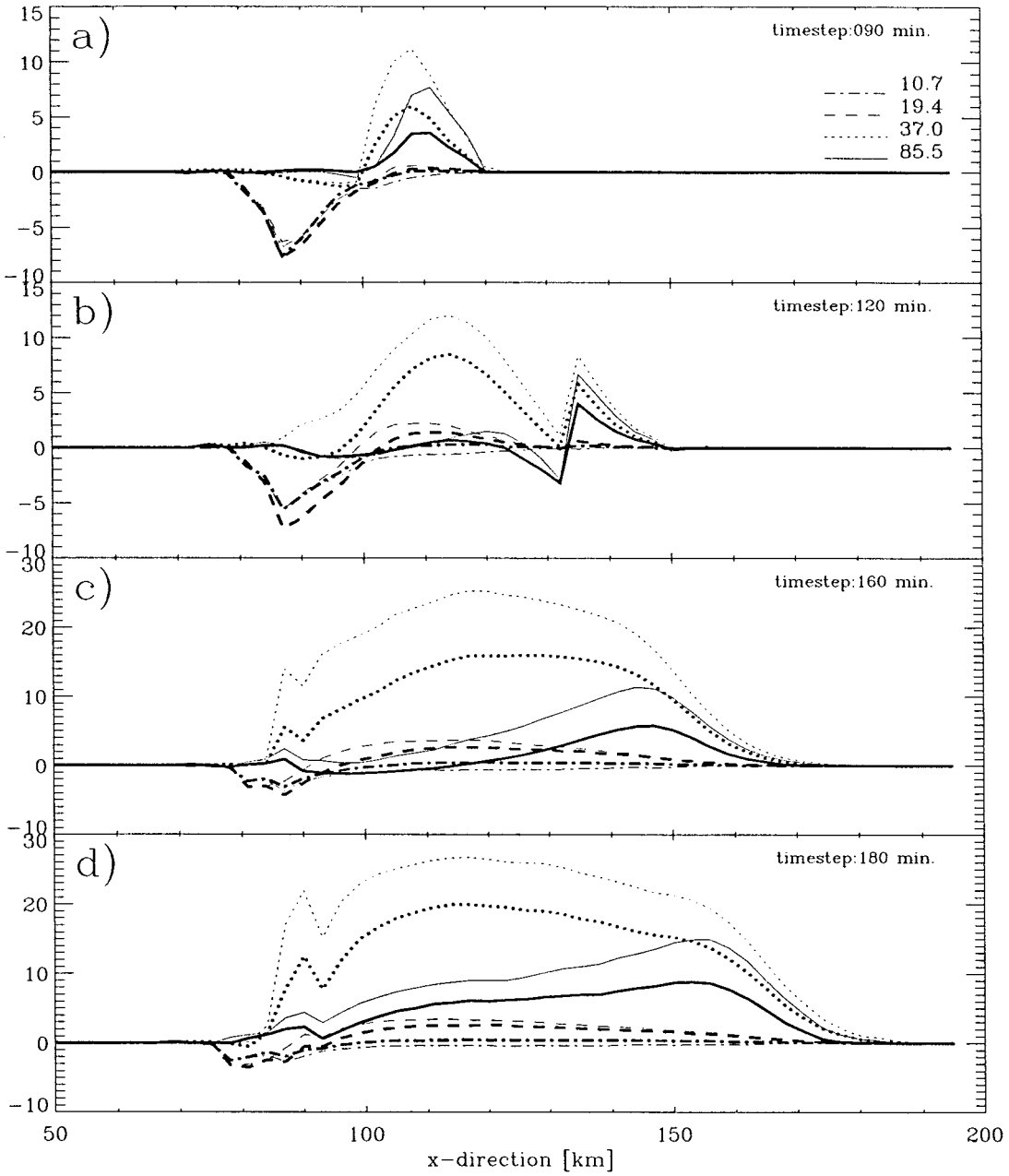

FIG. 10. ΔT_B for four model time steps at 10.7, 19.35, 37.0, and 85.5 GHz for particle permittivity model ML00 at nadir view over ocean for snow[1] size–density distribution. (Thick lines represent similar calculations for exponential particle size distributions.)

the PDSD because less scattering by large snowflakes occurs.

In the stratiform portion but close to the convective core (Figs. 12j,m), liquid EDSD are pretty well represented by PDSD, which deteriorate increasingly with distance from convection (Figs. 13j,m). In the remote stratiform part, small drops evaporate and lead to a shift of size distributions toward large masses. Above the FL, large liquid water amounts are available at $x = 93$ km, which became converted into frozen hydrometeors and precipitated farther away at $x = 120$ km and at later cloud development stages (Figs. 12a,d,g vs Figs. 13a,d,g). The spectra of frozen particles show an obvious discrepancy since at lower altitudes the parameterization strongly overestimates the number concentrations of small particles and underestimates those of larger particles. This effect becomes continuously less problematic toward the cloud top as shown by comparing Figs. 12b, 12e, and 12h. The reason is the collection/aggregation of small particles during sedimentation into

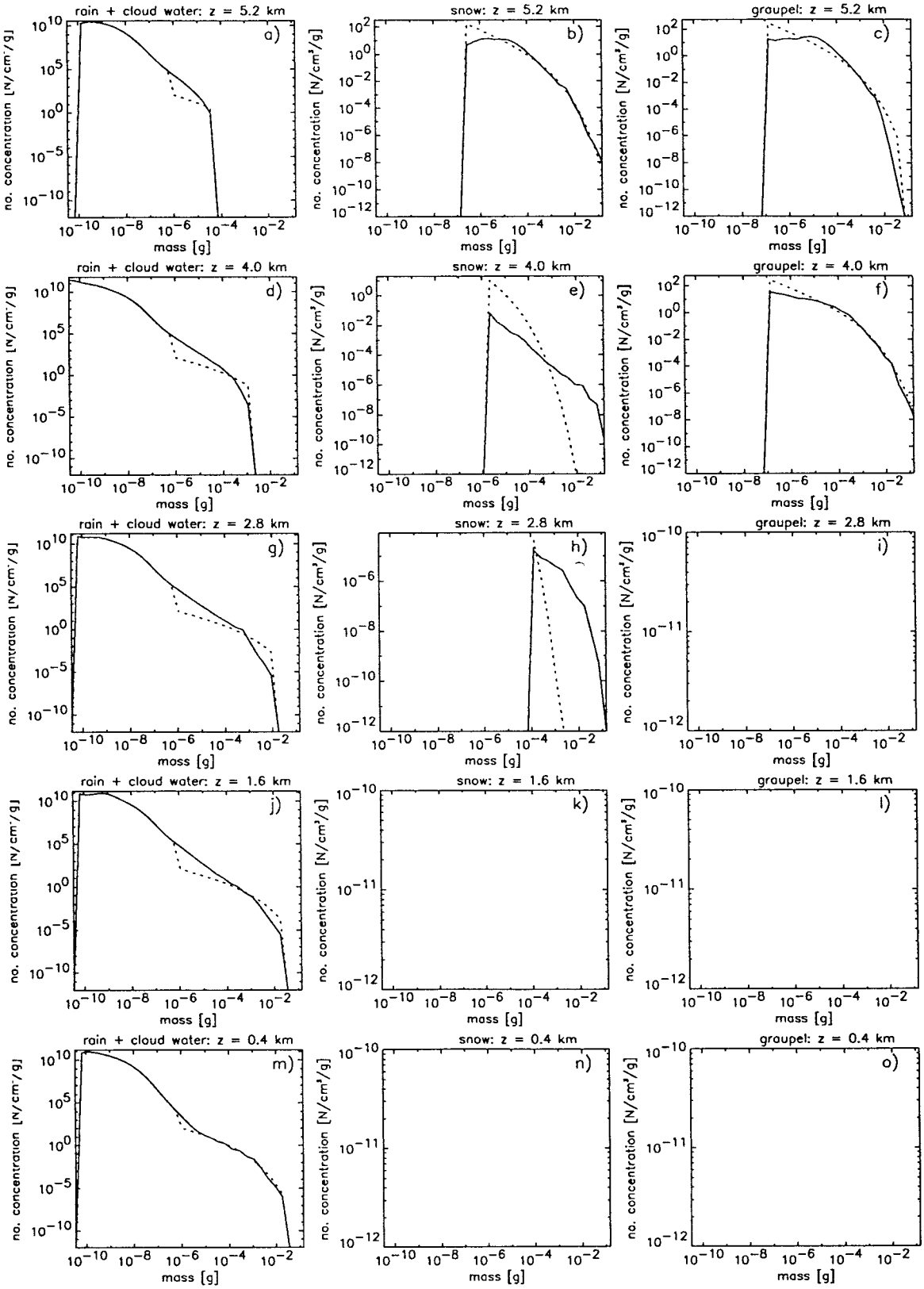

FIG. 11. Explicit particle number concentration spectra for (left column) liquid water, (middle column) snow, and (right column) graupel at five different altitudes at model time step $t = 120$ min and $x = 75$ km. Dashed lines indicate exponential size distributions matched to conserve liquid and ice water contents, respectively.

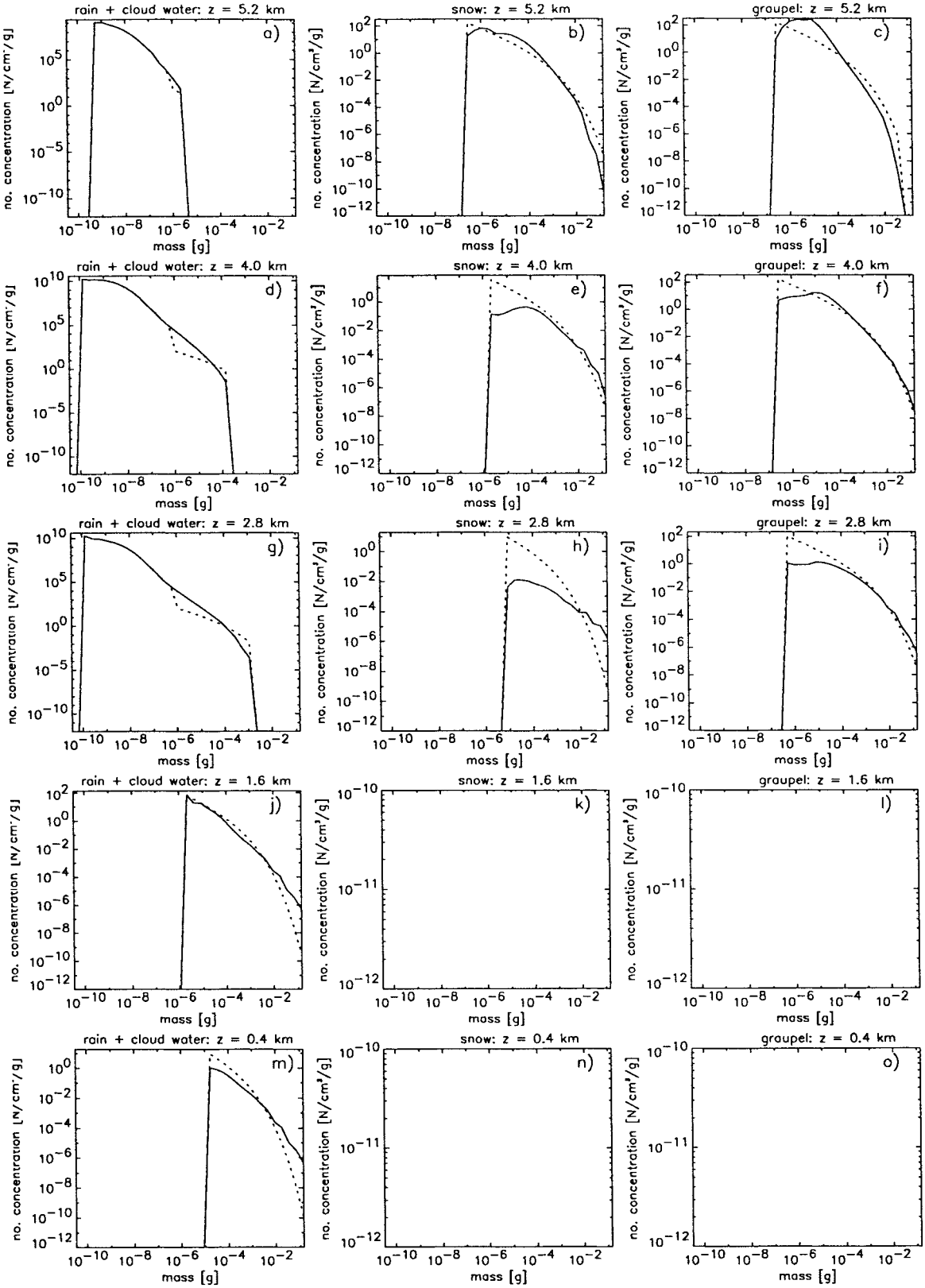

FIG. 12. Same as Fig. 11 but for model time step $t = 120$ min and $x = 93$ km.

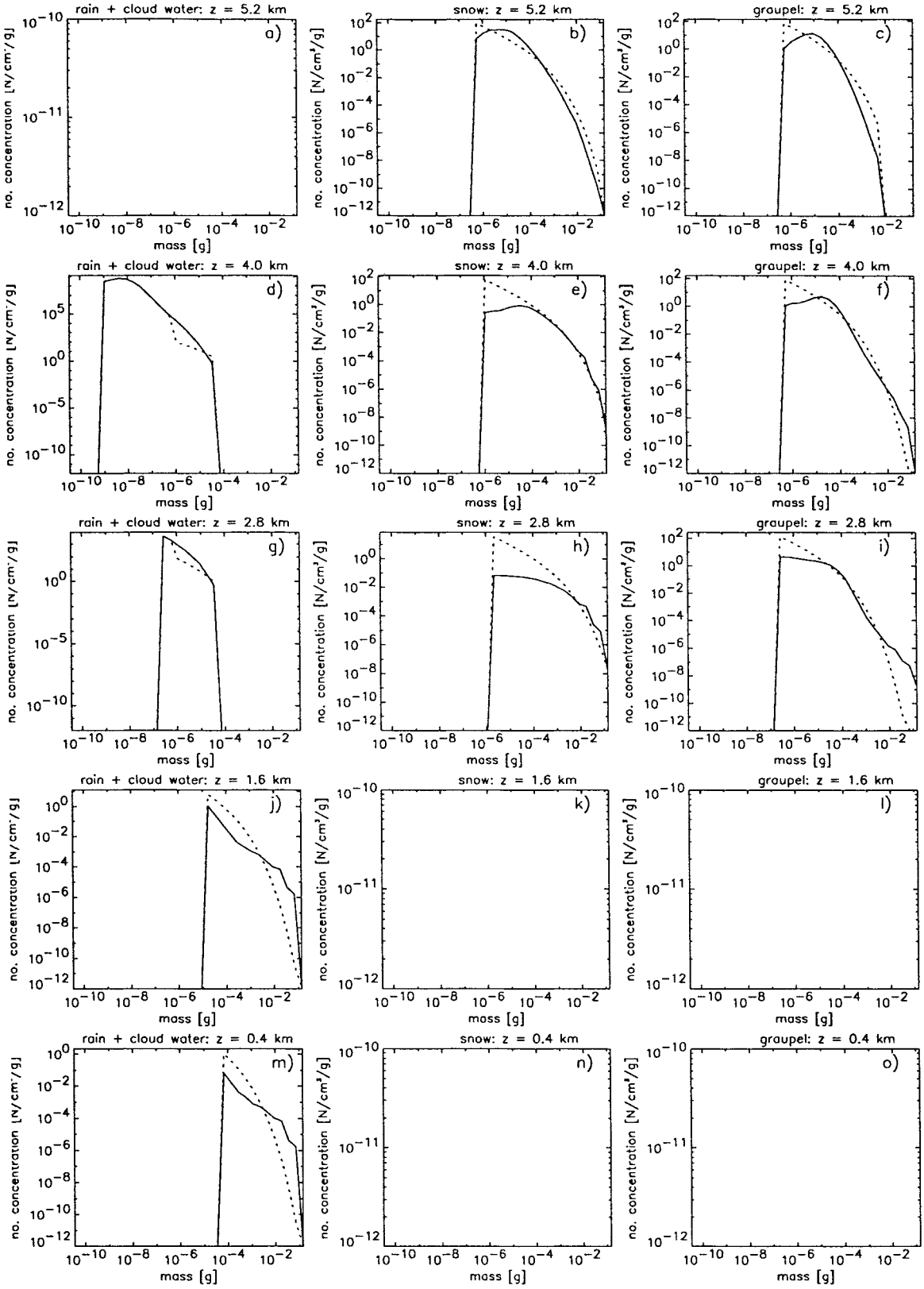

FIG. 13. Same as Fig. 11 but for model time step $t = 180$ min and $x = 120$ km.

lower layers. Since the exponential size distributions maintain the ice water content with a constant N_0, the reduction of small particle numbers is equalized at the expense of large particles by generating steeper slopes (parameter Λ).

When parameterized and explicit spectra are compared (Figs. 9a,b and Figs. 9c,d), lower average ΔT_Bs are observed for the PDSD. This is caused by the general overestimation of small particle numbers and underestimation of large particle numbers concerning all particle types by PDSD in the stratiform cloud portion leading to lower (excess) emission in the melting and liquid portions but less scattering above the FL. These effects cancel so that no net change in T_B is observed (see ML00 in Fig. 9a vs 9c). However, excess emission will be dominant at lower frequencies while excess scattering will be evident at higher frequencies. The MG_{wi} still produces too high ΔT_Bs for low densities. These differences are present over the whole computation domain and do not change with cloud evolution (see Fig. 10).

The superposition of effects from different particle spectra and melting model implementations suggest that for low particle densities (large particles) the melting effect dominates for all permittivity models. When Figs. 9c and 9e are compared, no obvious differences for both average ΔT_B and standard deviations are observed. When densities are higher, an average between the melting effect and the size distribution effects is noticed for ML96 and ML00, while MG_{wi} consistently suppresses size distribution signatures.

5. Summary and conclusions

As improvements in the technical performance of spaceborne sensors for cloud and rain microphysics sensing are achieved, better descriptions of important cloud features are required, which so far have been neglected. This is essential for database generation from combined radiative transfer–cloud model simulations for global retrievals of both hydrometeor properties and latent heating profiles, for tropical and extratropical conditions.

The important issue of this work was to employ a dataset that provided a consistent set of hydrometeor distributions with as few free parameters as possible. Experience from numerous radar studies (e.g., Meneghini et al. 1997) shows that by adjustment of particle density, size distribution, and particle permittivity, most measured vertical radar reflectivity profiles are reproducible; however, coincident passive microwave measurements may be difficult to match with model results using the constraints obtained from the radar inversion, particularly when a wider frequency range is covered. The incorporated particle properties are always parameterized and difficult to evaluate individually against each other. Thus the output from the spectral cloud model with a seven hydrometeor class model taken for the presented study provided a unique dataset to evaluate current assumptions about the radiative effect of melting particles. Apart from the melting effect, the availability of explicitly calculated spectra allows an assessment of the general representativity of exponential size distributions for precipitating hydrometeor spectra.

The four model cloud evolution states selected are mainly characterized by a stratiform outflow behind a strong convective cell located over a coastline in the eastern Mediterranean Sea driven by eastward directed winds. Rain rates decreased with increasing distance from the convective cell with average surface amounts of 1–3 mm h^{-1} in the stratiform area. Those cloud model layers, representing the altitude range within which melting occurs, were replaced by a melting model that was adjusted to match particle mass fluxes at the original levels above and below in order to maintain consistency with the cloud model output. This adjustment was restricted to profiles where vertical velocities were negligible. The model environment was completed by implementation of various particle permittivity models embedded in a radiative transfer code applicable to simulations along vertical or inclined optical paths over water and land surfaces.

Over land surfaces, no significant radiative signatures of the melting layer for downward looking radiometers could be identified. Independent of both size–density or permittivity model considerations, changes in brightness temperatures were below 8 K and thus below effects induced by other microphysical features and surface effects. Over water, the radiative effects were found to be attributed to the increase of emission when large frozen particles become wet and act radiometrically as huge raindrops. The quantities depend on particle size and particle composition, that is, particle permittivity. The widely used Maxwell–Garnett formulation, assuming particles composed of a water matrix with air/ice inclusions, seemed to exaggerate the melting effect, in particular when particles become rather large. Random-mixture particle models produced more realistic signatures. However, when only small particles are present, no significant effect was observed either with respect to the radar reflectivity or the passive microwave emission. At higher frequencies, attenuation of the melting layer emission by liquid water above the freezing level may reduce the net effect considerably. At the edge of overlying cloud layers containing supercooled water, relative changes of 75% were found between attenuated and unattenuated signatures.

A change of particle size–density parameterizations allowed the evaluation of size versus permittivity model influence. Since snow produced the largest particle mass fluxes above the FL, its size and density-dependent melting behavior could be expected to drive the radiative signature of the melting layer. Employing two different size–density adjustments—for example, the original model inherent low dry snowflake density of 0.01 g cm^{-3} versus a size-dependent parameterization developed by Klaassen (1988)—drastic differences between

simulations of the layers' optical properties, radar reflectivities, and radiation emission became apparent.

Particle permittivity model ML96 produced only minor effects at any density configuration with maximum ΔT_Bs (melting − no melting) never exceeding 10 K at 85.5 GHz and even less at other frequencies. These results and the fact that ML96 was developed for a single low frequency suggest its application with care. Based on the experience from numerous studies of radar return response to melting layer environments, the combination of 1) ML00 and low particle densities (thus large particles) showed realistic simulations as did 2) the classic Maxwell–Garnett model assuming ice inclusions in water matrices for moderate to high particle densities (thus smaller particles). For both configurations, the radar reflectivities at 13.8 GHz and brightness temperatures at 37.0 and 85.5 GHz were almost identical, while the second configuration produced consistently higher brightness temperatures at low frequencies. This leads to the conclusion that these frequencies seem crucial for the interpretation of active and passive measurements with respect to the melting layer. Once a bright band is visible from the radar measurements with multifrequency radiometry showing a considerable increase of emission at all frequencies, particles could be considered as wet (like water-coated) with moderate sizes. If at lower frequencies the radiometric effect is negligible, particles may be large but in a rather homogeneous ice–water mixture state. This knowledge may also be used to describe the melting stage; however, the simulations presented in this paper suggest that simultaneous hydrometeor sampling and radiometric measurements including higher frequencies (>90 GHz) are required for further analysis. Here, the density–size dependence is one of the key parameters.

In summary, the following conclusions from the available permittivity models, versus observations of melting behavior (e.g., Mitra et al. 1990; Knight 1979), can be drawn.

- Particle size and density are key parameters for the description of melting behavior (melting speed).
- Melting snow can be expected to have a larger effect compared to graupel because snowflake diameters are well above drop diameters and densities are generally low (and decrease with size); then wet snowflakes have electrical properties as oversized raindrops leading to excess microwave emission and reflectance.
- Current particle permittivity models represent a compromise because they only describe average properties and may not be accurate at individual particle-type–melting-stage configurations.
- The experimental studies of Mitra et al. (1990) of snowflake morphology during melting suggest that the primary meltwater is accumulated near the particles' surface. Thus its permittivity would be underestimated by ML00 and best approximated by MG_{wi}, while at later stages ML00 would be realistic. Thus ML00 represents a lower limit of possible effects once melting particles are present.

Another important issue in this context was the investigation of the applicability of parameterized size distribution functions since current three-dimensional cloud models only provide bulk quantities that require parameterized spectra to allow radiative transfer calculations. Thus explicit model spectra were replaced by the widely used exponential size distribution type with fixed intercept as obtained from adjustment to the model-derived liquid and ice water contents.

In all cases, these spectra showed a considerable underestimation of large and overestimation of small particle number concentrations for rain, snow, and graupel at those altitudes where particles are found after significant sedimentation time, that is, near the surface for raindrops and near the freezing level for snow and graupel. This is due to the general decrease of small drop numbers due to evaporation during their lifetime below the freezing level and the collection of small frozen particles by larger particles above the freezing level. When the liquid and ice water contents do not change drastically during these processes, the slope of the exponential size distributions remains constant and does not represent the redistributions of water within the spectra. The relative melting effect can be reduced by up to 40% due to the lack of large particles, which were found to produce the greatest response with respect to both radar reflectivity and emitted radiation.

Acknowledgments. The authors wish to thank Brad Ferrier (NASA) for his infinitely patient discussions of cloud microphysics and parameterization issues as well as Bill Olson and James Weinman (NASA) for advice concerning all aspects of the problem. This research was funded by the Deutsche Agentur fuer Raumfahrtangelegenheiten (DARA) under Contract AN-50 EE 9501-ZK and the European Space Agency (ESA) under Contracts 11947/96/NL/CN and 9122/97/NL/NB. This research was carried out during a visit at NASA Goddard Space Flight Center that was supported by the TRMM research program.

REFERENCES

Bauer, P., and N. C. Grody, 1995: The potential of the combination of SSM/I and SSM/T2 data to improve the identification precipitation and snowcover. *IEEE Trans. Geosci. Remote Sens.*, **33,** 252–261.

——, L. Schanz, and L. Roberti, 1998: Correction of three-dimensional effects for passive microwave remote sensing of convective clouds. *J. Appl. Meteor.*, **37,** 1619–1632.

——, J. P. V. Poiares Baptista, and M. de Iulis, 1999: On the effect of the melting layer on the microwave emission of clouds over the ocean. *J. Atmos. Sci.*, **56,** 852–867.

Berry, E. X, and R. L. Reinhardt, 1974: An analysis of cloud drop growth by collection. Part I: Double distributions. *J. Atmos. Sci.*, **31,** 1814–1824.

Bohren, C. F., and L. J. Battan, 1982: Radar backscattering of microwaves by spongy ice spheres. *J. Atmos. Sci.*, **39,** 2623–2628.

Dissanayake, A. W., and N. J. McEwan, 1978: Radar and attenuation properties and bright band. IEE Conf. Publ. 169-2, Institution of Electrical Engineers, Stevenage, United Kingdom, 328 pp.

Khain, A. P., and I. Sednev, 1995: Simulation of hydrometeor size spectra evolution by water–water, ice–water and ice–ice interactions. *Atmos. Res.,* **36,** 107–138.

——, and ——, 1996: Simulation of precipitation formation in the Eastern Mediterranean coastal zone using a spectral microphysics cloud ensemble model. *Atmos. Res.,* **43,** 77–110.

——, ——, and V. Khvorostyanov, 1996: Simulation of coastal circulation in the eastern Mediterranean using a spectral microphysics cloud ensemble model. *J. Climate,* **9,** 3298–3316.

Klaassen, W., 1988: Radar observations and simulation of the melting layer of precipitation. *J. Atmos. Sci.,* **45,** 3741–3753.

Knight, C. A., 1979: Observations of the morphology of melting snow. *J. Atmos. Sci.,* **36,** 1123–1130.

Kummerow, C., 1993: On the accuracy of the Eddington approximation for radiative transfer at microwave frequencies. *J. Geophys. Res.,* **98,** 2757–2765.

Liebe, H. J., P. Rosenkranz, and G. A. Hufford, 1992: Atmospheric 60 GHz oxygen spectrum: New laboratory measurements and line parameters. *J. Quant. Spectrosc. Radiat. Transfer,* **48,** 629–643.

Magono, C., and T. Nakamura, 1965: Aerodynamic studies of falling snowflakes. *J. Meteor. Soc. Japan,* **43,** 139–147.

Meneghini, R., and L. Liao, 1996: Comparisons of cross sections for melting hydrometeors as derived from dielectric mixing formulas and a numerical method. *J. Appl. Meteor.,* **35,** 1658–1670.

——, and ——, 1998: Effective dielectric constants of melting hydrometeors and their use in radar bright-band models. *Proc. Int. Geoscience and Remote Sensing Symp.,* Seattle, WA, IEEE, 147–149.

——, and ——, 2000: Effective dielectric constants of mixed-phase hydrometeors. *J. Atmos. Oceanic Technol.,* in press.

——, H. Kumagai, J. R. Wang, T. Iguchi, and T. Kozu., 1997: Microphysical retrievals over stratiform rain using measurements from an airborne dual-wavelength radar-radiometer. *IEEE Trans. Geosci. Remote Sens.,* **35,** 487–506.

Mitra, S. K., O. Vohl, M. Ahr, and H. R. Pruppacher, 1990: A wind tunnel and theoretical study of the melting behavior of atmospheric ice particles. IV: Experiment and theory for snow flakes. *J. Atmos. Sci.,* **47,** 584–591.

Rutledge, S. A., and P. V. Hobbs, 1983: The mesoscale and microscale structure and organization of clouds and precipitation in midlatitude cyclones. VIII: A model for the ''seeder-feeder'' process in warm-frontal rainbands. *J. Atmos. Sci.,* **40,** 1185–1206.

Schluessel, P., and H. Luthardt, 1991: Surface wind speeds over the North Sea from Special Sensor Microwave/Imager observations. *J. Geophys. Res.,* **96,** 4845–4854.

Schols, J. L., J. A. Weinman, R. E. Stewart, and R. P. Lawson, 1995: The retrieval of dry and wet snow distributions from SSM/I measurements and MM5 forecast results. *Proc. Int. Geoscience and Remote Sensing Symp.,* Florence, Italy, IEEE, 887–889.

——, ——, G. D. Alexander, R. E. Stewart, L. J. Angus, and A. C. L. Lee, 1999: Microwave properties of frozen precipitation around a North Atlantic cyclone. *J. Appl. Meteor.,* **38,** 29–43.

Vivekanandan, J., J. Turk, G. L. Stephens, and V. N. Bringi, 1990: Microwave radiative transfer studies using combined radar and radiometer measurements during COHMEX. *J. Appl. Meteor.,* **29,** 561–585.

Wexler, R., 1995: The melting layer. Blue Hill Observatory and Harvard University Meteorological Radar Studies No. 3., 29 pp. [Available from Harvard University, Blue Hill Observatory, Milton, MA 02186.]